Muonium state exchange dynamics in *n*-type GaAs

K. Yokoyama [1,*] J. S. Lord [1] P. W. Mengyan [2] M. R. Goeks [2] and R. L. Lichti [3]
[1]*ISIS Neutron and Muon Facility, STFC Rutherford Appleton Laboratory, Didcot OX11 0QX, United Kingdom*
[2]*Department of Physics, Northern Michigan University, Marquette, Michigan 49855, USA*
[3]*Department of Physics and Astronomy, Texas Tech University, Lubbock, Texas 79409-1051, USA*

(Received 31 August 2023; accepted 11 July 2024; published 6 August 2024)

Muonium (Mu), a pseudoisotope of hydrogen with a positively charged muon in place of the proton, takes the form $Mu^{+,0,-}$ (like isolated hydrogen, i.e., $H^{+,0,-}$) in semiconductors. The specifics of the charge state depend on the local electronic environment of the host. After initial muon implantation, generated Mu centers interact with free charge carriers and electronic spins, transition between sites, and form a dynamic network of state exchange. We identified the model of Mu dynamics in *n*-type GaAs using the density matrix simulation method and photoexcited muon spin spectroscopy technique. Fitting to the dark and illuminated μSR data provided transition rates between Mu states, revealing the underlying mechanisms at play between the Mu centers (cf. isolated H) and the host. Deduced capture/scattering cross sections of the Mu states reflected the microscopic dynamics of Mu. Illumination studies enabled us to measure interactions between Mu and minority carriers, which would be unavailable in dark measurements without heating. The methodology developed in this study may be applied to other semiconductor systems for a deeper understanding of the Mu state exchange dynamics.

DOI: 10.1103/PhysRevResearch.6.033140

I. INTRODUCTION

Isolated hydrogen (H) is an essential impurity to understand for semiconductor engineering due to its ubiquity, fast diffusion, high reactivity, and in semiconductors its propensity for modifying the host's electrical and optical properties either beneficially (e.g., passivating dangling bonds in bulk and on surfaces) or detrimentally (e.g., passivating intentional dopant atoms) [1]. Investigating isolated H atoms is thus important yet difficult, since they often transition rapidly from their precursor to final stable states. Few experimental techniques can overcome these challenges in studying isolated H including, for instance, deep level transient spectroscopy [2], vibrational spectroscopy [3], and muon spin spectroscopy (muon spin rotation, relaxation, and resonance; collectively μSR) [4–7]. Since a positively charged muon μ^+ has 1/9th the proton mass and a 2.2 μs mean lifetime, muonium ($Mu^{+,0,-}$) is an experimentally accessible analog of isolated hydrogen ($H^{+,0,-}$) in materials. Hence, μSR has made significant contributions in this avenue by investigating the electronic structure and dynamics of Mu states.

Four Mu states, Mu_T^0, Mu_{BC}^0, Mu_T^-, and Mu_{BC}^+ are commonly found in tetrahedral semiconductors, including the diamond structured elemental semiconductors (e.g., Si, Ge) and the related zinc-blende and wurtzite compounds (e.g., GaAs, CdS). Of these states, the first two are paramagnetic Mu^0 ($\mu^+ + e^-$) states characterized by their hyperfine (HF) coupling [4–7], and the latter two show compensation analogous to H [8] as Mu^- ($\mu^+ + 2e^-$) in *n*-type and Mu^+ (singly ionized Mu^0) in *p*-type materials under equilibrium conditions [9,10]. Mu_T^0 is a compact Mu state huddling at the tetrahedral interstitial site. It generally has a large isotropic HF constant A_μ (i.e., ∼GHz), and can rapidly diffuse through a crystal lattice by hopping through equivalent sites. In contrast, Mu_{BC}^0 is known to be much less diffusive and localized at the bond-center site. It has an anisotropic HF constant axially symmetric about ⟨111⟩, with $A_\parallel$ and $A_\perp$ representing components parallel and perpendicular to the ⟨111⟩ axis respectively. Its electronic orbital is extended to the crystal lattice with a higher probability on neighboring atoms, resulting in both $A_\parallel$ and $A_\perp$ roughly an order of magnitude (or two) smaller than A_μ. Note that the HF constants of Mu_T^0 and Mu_{BC}^0 being smaller than the HF constant of the vacuum state (4.46 GHz) implies some delocalization of the electronic orbital onto the host crystal lattice. Hence, accommodating Mu_T^0 or Mu_{BC}^0 generally requires deformation of a crystal lattice. For Mu_T^0, the lattice distortion plays a key role in understanding its diffusion behavior. Indeed, the Mu_T^0 state in semiconductors/insulators has provided an ideal test ground for the small-polaron theory [11]. For Mu_{BC}^0, its formation can elongate the bond length 30–40% according to computational studies [6].

A Mu center can dynamically change its state from one to another; this includes a site change of a neutral state (e.g., Mu_{BC}^0 converted to Mu_T^0) and a charge-state change upon interacting with free carriers[1] In addition, a bound electron

*Contact author: koji.yokoyama@stfc.ac.uk

[1]Here, the reader should not confuse the site change interaction with the hopping motion of Mu_T^0. The latter describes a phonon-assisted motion of Mu_T^0 hopping between nearby equivalent sites.

in a neutral state can undergo spin exchange interaction with free electrons. These interactions often form a cyclic network [5,12] and have been extensively studied in Si using the radio-frequency μSR technique, where Mu states are selectively measured in resonant conditions [13,14]. More recently, transition dynamics enhanced by generated excess charge carriers in optically pumped Si and Ge wafers were studied via the photoexcited μSR (photo-μSR) technique [15–20]. A distinct advantage of *pulsed* photo-μSR is generating excess carriers without heating samples, thereby maintaining constant band-gap energies. Other recent studies have applied density matrix methods and successfully calculated the time evolution of a muon spin ensemble in the cyclic models, giving a rate for each transition channel [17,18]. If a state exchange process involves a free carrier (e.g., $\mathrm{Mu}_\mathrm{T}^0 + e^- \rightarrow \mathrm{Mu}_\mathrm{T}^-$), its capture cross section can be calculated from an obtained transition rate. Therefore, these measurements provide valuable insights into interactions between isolated H and charge carriers, which are otherwise extremely difficult (if not impossible) to study.

II. DARK MEASUREMENTS AND DENSITY MATRIX SIMULATIONS

In this article, we report both dark and illuminated μSR measurements on *n*-type GaAs (n-GaAs) and explain the Mu transition dynamics using the density matrix method. Generally, μSR data from semiconductors are a convolution of Mu states and their dynamics. The analysis presented here deconvolutes the data into each component to understand the underlying mechanisms. We also demonstrate that illumination by monochromatic laser light provides precise control of an excess carrier density Δn, allowing us to excite some of the transition channels in the cyclic model which are inaccessible in dark measurements without heating the sample. The discovered model in *n*-GaAs turns out to be simpler than the case of Si or Ge, and can be considered as a basic system of Mu involved in exchange interactions with free carriers.

The experiment was carried out using the high magnetic field (HiFi) μSR spectrometer [21] at the ISIS Pulsed Neutron and Muon Source at the STFC Rutherford Appleton Laboratory in the UK [22]. A detailed discussion of the illumination facility and associated equipment is available elsewhere [23]. This experiment used a single crystal *n*-GaAs (Si doped; average carrier concentration of $N_\mathrm{d} = 2.5 \times 10^{16}$ cm^{-3}) with a diameter of 50 mm, thickness of 450 μm, and ⟨100⟩ crystal axis perpendicular to the surface. The wafer was single-side polished. Laser light illuminated the polished side, and any transmitted light was scattered on the other side, where the surface was chemically etched. The sample was contained in a helium-gas purged sample cell mounted on a closed cycle refrigerator. The gas purged construction ensured uniform and mechanical stress-free cooling. On the sample cell, muons were implanted on the wafer's etched side through a titanium window (100 μm thick), while laser light propagating in the opposite direction illuminated the sample from the other side through a glass window [23]. Aluminum sheet degraders were used to adjust the implantation depth of the muons (with a kinetic energy of 4 MeV) such that the muon distribution profile was centered in the wafer [24].

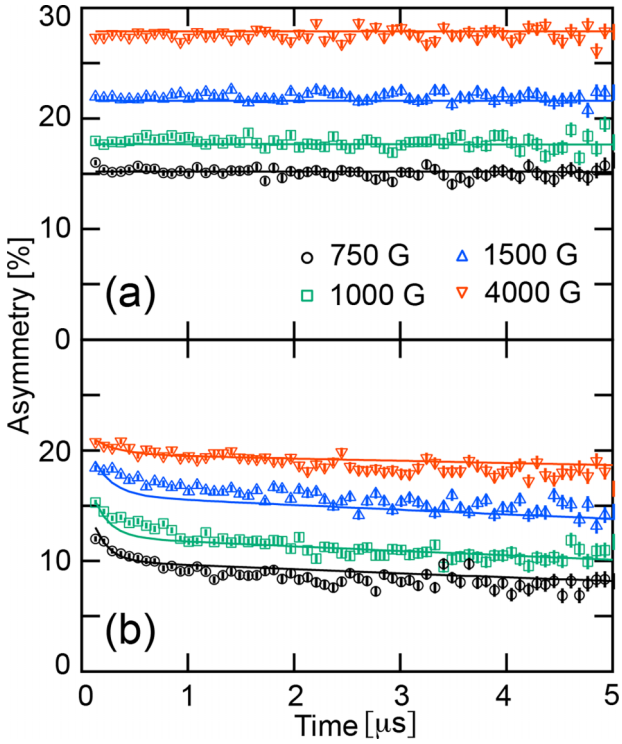

FIG. 1. μSR time spectra measured in dark at (a) 290 K and (b) 20 K under four representative fields. Five million muon decay events were averaged for each spectrum. The full muon asymmetry in HiFi is ∼28%. Solid lines denote the fit result (see text).

First, we carried out measurements in dark conditions to find a single model that can describe μSR time spectra in the entire temperature range. Figures 1(a) and 1(b) show the μSR spectra at 290 and 20 K respectively under four representative longitudinal fields (LF), where the field vector is parallel to the initial muon spin. At 290 K, the time spectra show no relaxation. Increasing the magnitude of the applied LF shows a recovery of the spin polarizaton that Kadono *et al.* attributed to a precursor Mu state, presumably Mu_T^0, rapidly converted to the stable Mu_T^- state upon capturing a free electron [25]. The time spectra appear to be flat because spin relaxation in the precursor state and the subsequent state conversion are too fast to observe at a pulsed muon facility. In contrast, a relaxing component appears at 20 K that was (in the literature) attributed to spin relaxation in the $\mathrm{Mu}_\mathrm{BC}^0$ state, which was considered to be more predominant in low temperatures because of the metastability of the $\mathrm{Mu}_\mathrm{BC}^0$ center in GaAs. As the temperature (T) rises, the transition rate from $\mathrm{Mu}_\mathrm{BC}^0$ to Mu_T^0 increases [25].

On the basis of these previous works, we developed a model shown in Fig. 2(a), where three Mu centers are involved. Here, transitions between Mu_T^0 and Mu_T^- require capturing a free charge carrier: $\mathrm{Mu}_\mathrm{T}^0 + e^- \rightarrow \mathrm{Mu}_\mathrm{T}^-$ and $\mathrm{Mu}_\mathrm{T}^- + h^+ \rightarrow \mathrm{Mu}_\mathrm{T}^0$ (or releasing an electron spontaneously, $\mathrm{Mu}_\mathrm{T}^- \rightarrow \mathrm{Mu}_\mathrm{T}^0 + e^-$). The site change interaction between $\mathrm{Mu}_\mathrm{BC}^0$ and Mu_T^0 requires phonons to overcome the energy barrier. For the $\mathrm{Mu}_\mathrm{BC}^0$ and Mu_T^0 centers, spin exchange interaction can take place between a bound and conduction electron, resulting in a muon spin relaxation due to HF interaction [24].

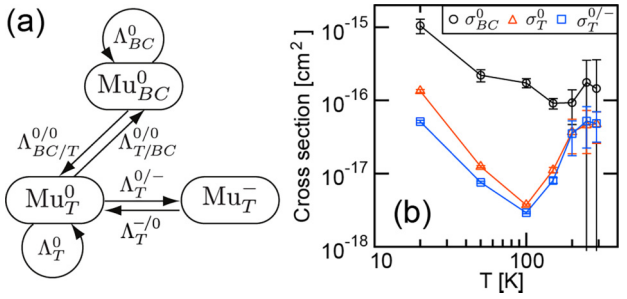

FIG. 2. (a) The model of Mu state exchange in n-GaAs. A superscript and subscript of Λ indicate the charge state and Mu site respectively, with a slash between before and after a transition. (b) Temperature dependence of scattering/capture cross sections. Straight lines connecting points are a guide to the eye.

Positively charged Mu^+_{BC} states are energetically unfavorable in n-type samples [4–7] and hence not included in the model. Each state exchange is characterized by a transition rate Λ. Similarly, the spin exchange interaction in Mu^0_{BC} and Mu^0_T are characterized by Λ^0_{BC} and Λ^0_T respectively. Density matrix calculations on this model were applied to fit the measured μSR time spectra.

The calculation was carried out using QUANTUM, a Python program to solve the time evolution of the muon spin using the density matrix method [26]. The program generates a full Hamiltonian for a given system and diagonalizes it to obtain eigenvectors and eigenstates. The density matrix evolves with time, which can then be used to calculate the muon spin evolution [5].[2] For a system with spin flips and state changes, the program calculates a matrix describing the evolution of the density matrix. The transitions take place randomly with a uniform rate. A representative source code and details of the fitting procedure are provided in the Supplemental Material [27]. Briefly, the code builds a system described in Fig. 2(a), which is made only of muons and electrons. Then, QUANTUM simulates the time evolution after an initial distribution of the Mu states. In the code, a fractional yield of Mu^0_T upon muon implantation, $f(Mu^0_T)$, is a fit parameter, but $f(Mu^0_{BC})$ is a dependent variable determined by $f(Mu^0_{BC}) = 1 - f(Mu^0_T)$; $f(Mu^-_T)$ is assumed to be zero initially because Mu^-_T is a product of Mu^0_T upon an electron capture event. For Mu^0_T and Mu^0_{BC}, their muon spin interacts with the bound electron via the HF constants, i.e., $A_\mu = 2.88$ GHz, $A_\parallel = 217.8$ MHz, and $A_\perp = 87.7$ MHz [4]. The Mu states are assumed to have no interaction with nearby nuclear spins. Here, for simplicity in the computation, we exclude low-field data and use only the high-field data for fitting, where the muon spin is decoupled from nuclear dipole and quadrupole moments in the system [28]. Hence, the system's interactions with the bath take place incoherently only via the electron spin relaxation and state transitions. Note that diffusive motions of Mu (e.g., Mu^0_T hopping) are not part of the model. However, obtained spin relaxation and state transition rates can carry contribution from the hopping motion (see below). The modeling takes account of the Zeeman interaction with an applied field (a given parameter in the fitting). Repolarization of the muon spin by the Zeeman effect plays a key role in differentiating the Mu states by the HF interaction. After a calculation, the program returns a normalized time domain signal (i.e., unity at t = 0), which is then multiplied by a scaling factor to match the measured μSR spectrum. The scaling factor is determined from the 290 K data because at room temperature (RT) the relaxing Mu^0_{BC} component is negligibly small and the muon signal is entirely diamagnetic. To improve the fitting accuracy, a global fit was performed on a set of high-LF data ranging between 500 and 4000 G.

Obtained fit results in Table I show how the Mu state exchange dynamics and spin relaxation manifest themselves in the μSR spectra in Fig. 1. At 290 K, all muons are initially in the Mu^0_T state [$f(Mu^0_T) \simeq 1$], which are subsequently rapidly depolarized via the spin exchange interaction (49 MHz) or converted to Mu^-_T (50 MHz). However, the backward transition, $Mu^-_T \rightarrow Mu^0_T$, rarely happens in this electron-rich environment. This behavior explains the repolarization by LF and the absence of relaxation in the observed time spectra. Large standard errors on Λ^0_{BC} and $\Lambda^{0/0}_{BC/T}$ reflect that $f(Mu^0_{BC}) \simeq 0$ at RT.[3] In contrast, at 20 K, a fraction of muons (34%) is in the Mu^0_{BC} state upon implantation but is rapidly depolarized via the spin exchange interaction (77 MHz) or converted to Mu^0_T (24 MHz). In this sample, the conduction electron density n_e at 20 K is 6.2×10^{15} cm^{-3}, compared to 2.2×10^{16} cm^{-3} at 290 K (see below for the calculation). This paucity and the slower thermal velocity of electrons at low temperatures result in slowing down Λ^0_T and $\Lambda^{0/-}_T$, and providing chances for Mu^-_T to spontaneously release one of its electrons (0.07 MHz) and go back to Mu^0_T, where the muon spin can be depolarized by the HF interaction. This mechanism is behind the slow relaxing tail observed in Fig. 1(b).

III. ELECTRON CAPTURE AND SCATTERING CROSS SECTIONS

Transition channels that involve charge carriers can be characterized by capture or scattering cross sections. Three transition rates in Table I can be described as follows:

$$\Lambda^0_T = n_e v_e \sigma^0_T, \tag{1}$$

$$\Lambda^{0/-}_T = n_e v_e \sigma^{0/-}_T, \tag{2}$$

$$\Lambda^0_{BC} = n_e v_e \sigma^0_{BC}, \tag{3}$$

where σ^0_T and σ^0_{BC} are an electron scattering cross section for Mu^0_T and Mu^0_{BC} respectively, and $\sigma^{0/-}_T$ is an electron capture cross section for the Mu^0_T center. An electron and hole thermal

[2]This is a quantum mechanical manipulation of $\vec{P}(t) = \langle \vec{\sigma}^\mu(t) \rangle = \mathrm{Tr}[\rho(t)\vec{\sigma}^\mu]$, where $\vec{P}$ and $\vec{\sigma}^\mu$ are the muon spin polarization and spin operator respectively, and ρ denotes the density matrix calculated from the Hamiltonian.

[3]Thus, fitting with both Λ^0_{BC} and $\Lambda^{0/0}_{BC/T}$ set to zero gives the same result.

TABLE I. Results of global fitting to the dark, LF-scan data measured at several temperatures. The unit of Λ's is MHz.

T (K])	$f(\mathrm{Mu}_\mathrm{T}^0)$	Λ_T^0	$\Lambda_\mathrm{T}^{0/-}$	$\Lambda_\mathrm{T}^{-/0}$	Λ_BC^0	$\Lambda_\mathrm{BC/T}^{0/0}$	$\Lambda_\mathrm{T/BC}^{0/0}$
290	0.99 ± 0.06	49 ± 22	50 ± 22	0.000 ± 0.001	147 ± 216	39 ± 55	0.0 ± 0.7
250	0.99 ± 0.07	44 ± 26	49 ± 28	0.000 ± 0.002	166 ± 168	74 ± 71	0.0 ± 0.9
200	0.86 ± 0.07	31 ± 15	29 ± 15	0.000 ± 0.002	78 ± 39	21 ± 10	0.0 ± 0.6
150	0.53 ± 0.01	8.0 ± 0.7	5.7 ± 0.5	0.000 ± 0.002	65 ± 11	16 ± 3	0.00 ± 0.02
100	0.73 ± 0.01	2.10 ± 0.06	1.64 ± 0.05	0.055 ± 0.002	97 ± 14	20 ± 4	0.132 ± 0.007
50	0.75 ± 0.01	4.3 ± 0.1	2.6 ± 0.1	0.077 ± 0.002	75 ± 14	19 ± 4	0.123 ± 0.008
20	0.66 ± 0.02	10.0 ± 0.5	3.8 ± 0.2	0.074 ± 0.002	78 ± 17	24 ± 7	0.07 ± 0.01

velocity, v_e and v_h respectively, can be calculated from the equipartition theorem (v_h will be required later),

$$v_e = \sqrt{\frac{3k_BT}{m_e}}, \tag{4}$$

$$v_h = \sqrt{\frac{3k_BT}{m_h}}, \tag{5}$$

where k_B is the Boltzmann constant, and m_e and m_h are the density of states' effective mass of electron and hole respectively. In GaAs, they are given by

$$m_e = 0.067m_0, \tag{6}$$

$$m_h = 0.48m_0, \tag{7}$$

where m_0 is the electron rest mass. Finally, n_e can be determined from the following equation, describing a ratio of the number of electrons in the donor state to the total number of electrons:

$$\frac{n_d}{n_d + n_e} = \frac{1}{1 + \frac{N_c}{2N_d}\exp\left[\frac{-(E_c - E_d)}{k_BT}\right]}, \tag{8}$$

where n_d is the electron density in the donor state, N_c is the effective density of states function in the conduction band, and $E_c - E_d$ is the ionization energy of the donor electrons. Using Eq. (8), one can calculate $n_e \simeq N_d(1 - \frac{n_d}{n_d+n_e})$ with $N_c = 4.7 \times 10^{17}$ cm^{-3}, $N_d = 2.5 \times 10^{16}$ cm^{-3}, and $E_c - E_d = 5.8$ meV. The derivation of Eq. (8) is available elsewhere [29].

The dark LF scan data were taken at seven temperatures (Table I). For each temperature, we applied the fitting procedure, obtained transition rates, and calculated the σ's. As a result, the temperature dependence of the cross sections was obtained as shown in Fig. 2(b). First, σ_T^0 and $\sigma_\mathrm{T}^{0/-}$ are an order of magnitude smaller than σ_BC^0 in this temperature range. This is considered as a manifestation of the physical size of the Mu_T^0 and $\mathrm{Mu}_\mathrm{BC}^0$ center, as discussed initially. The small cross sections of Mu_T^0 ($<10^{-16}$ cm^{-2}) are reasonable because it has very little spatial overlap with the wave function of conduction electrons (see next paragraph). In this context, we note that Chow *et al.* reported $\sigma_\mathrm{T}^{0/-} \sim 10^{-15}$ cm^{-2} [30]. We attribute this difference in cross-section to be rooted in the difference in temperature range; their measurement was carried out above 850 K, where free carriers are thermally excited across the band gap. Presumably, this large temperature difference effected marked differences in the temperature-dependent capture cross sections.

Second, it is notable that σ_T^0 and $\sigma_\mathrm{T}^{0/-}$ are at similar values and have the same characteristic temperature dependence with their minimum at about 100 K. This behavior should be contrasted with the temperature dependence of the Mu_T^0 hop rate measured in high-resistivity GaAs, which exhibited similar behavior and took its minimum value at 90 K [31]. Kadono *et al.* explained the behavior as above the crossover temperature T_X, the system is thermally activated and phonon-assisted tunneling is predominant; below T_X, incoherent quantum tunneling becomes a dominant process with decreasing temperature. In light of this diffusion mechanism, we considered the following hypothetical model and how it could manifest itself in the behavior of σ_T^0 and $\sigma_\mathrm{T}^{0/-}$. In the first place, the carrier and spin exchange interaction take place in a small volume where the electronic orbitals of Mu_T^0 and free carriers spatially overlap. This is schematically drawn in the bottom row of Fig. 3; the spatial overlap exists only under the vertical gray strips, which indicate a spread of carrier's wave function around the crystal lattice. At $T = T_\mathrm{X}$ [Fig. 3(b)], the spatial overlap is minimum because Mu_T^0 is localized at the center of the void. Its electronic orbital slightly deforms and pushes away the crystal lattice, making the overlapped volume even smaller. When thermally excited at $T > T_\mathrm{X}$ [Fig. 3(c)], the Mu_T^0 wave function spreads out. Hence, the overlapped volume becomes larger, and so does the cross section. In contrast, when the quantum tunneling becomes dominant at $T < T_\mathrm{X}$ [Fig. 3(a)], the Mu_T^0 wave

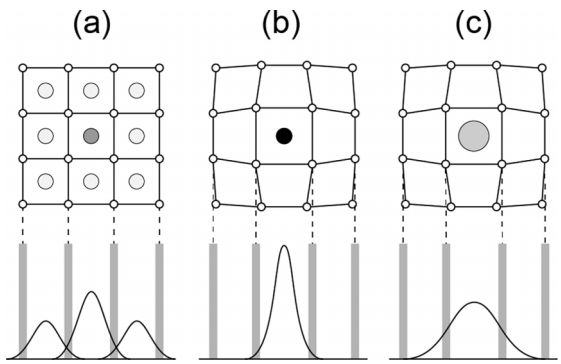

FIG. 3. Schematic diagrams showing Mu_T^0 in a crystal lattice (top row) and spatial distributions of its wave function (bottom row) for (a) $T < T_\mathrm{X}$, (b) $T = T_\mathrm{X}$, and (c) $T > T_\mathrm{X}$. In the top row, size and grayscale of the circles indicate their spread and probability amplitude respectively. In the bottom row, vertical gray strips indicate the crystal lattice through which the charge carriers are transported.

function is delocalized and forms peaks at nearby equivalent sites. A lower probability at its original position and the development of probabilities at the adjacent sites relax the lattice deformation; this effect presumably results in increasing the overlapped volume and in turn the cross section. A similar discussion may be applied to the temperature dependence of $\sigma^0_{\rm BC}$, which monotonically increases with decreasing temperature. In this case, $T_{\rm X}$ may be higher than $\mathrm{Mu}^0_{\rm T}$, and the increasing slope in the high-T side is not observable in our study because of the lower fractional yield of $\mathrm{Mu}^0_{\rm BC}$ above RT. The higher $T_{\rm X}$ can be associated with the $\mathrm{Mu}^0_{\rm BC}$ motion requiring more energy than $\mathrm{Mu}^0_{\rm T}$ because elongating the Ga-As bond upon $\mathrm{Mu}^0_{\rm BC}$ formation is more energetically costly [32]. Proving this model would require a computational approach, which is beyond the scope of this paper.

IV. ILLUMINATION MEASUREMENTS

In order to test the state exchange model and measure capture cross sections for holes, we performed photo-μSR studies on this sample. Previous studies on GaAs reported muon spin depolarization upon carrier generation by laser light [33]. Here, the arrival of a laser pulse was measured at the sample position and accurately timed with respect to the muon pulse [23]. The laser pulse delay Δt was set to 0.5 μs to have a dark period at the beginning of a time spectrum, to confirm experimental consistency with the fully dark measurements. Short carrier lifetimes in GaAs ($\lesssim 1$ ns) mean that carriers can interact with Mu only during the laser pulse duration, which is 8 ns FWHM in the setup. Hence, as shown in Fig. 4, the carrier-induced depolarization is observed as a step-like change in the time spectra. To maximize the signal, the pump wavelength needs optimization; if the photon energy $h\nu$ is too small compared with the gap energy $E_{\rm g}$, the sample becomes transparent for the wavelength and few carriers are generated. If, however, $h\nu$ is larger than $E_{\rm g}$, all photons are absorbed near the surface and there are no free carriers generated in the bulk. Thus, as shown in Fig. 5, a signal peak can be found in the wavelength scan where the spatial overlap of generated carriers and implanted muons is maximized. Since $E_{\rm g}$ is dependent on temperature, this measurement for an optimum wavelength was repeated at every temperature. The pump wavelengths 1.38 and 1.49 eV, for Figs. 4(a) and 4(b) respectively, were selected from this measurement. By virtue of the monochromaticity of laser light, the excess carrier density Δn can be calculated from a measured photon flux (typically, a pulse energy of ≈1 mJ illuminated an area of ≈5 cm^2 on the sample) and absorption coefficients [34].[4]

With these optical parameters, the photo-μSR time spectra shown in Fig. 4 were analyzed. For the RT data [Fig. 4(a)], the calculation included additional transition rates induced by the

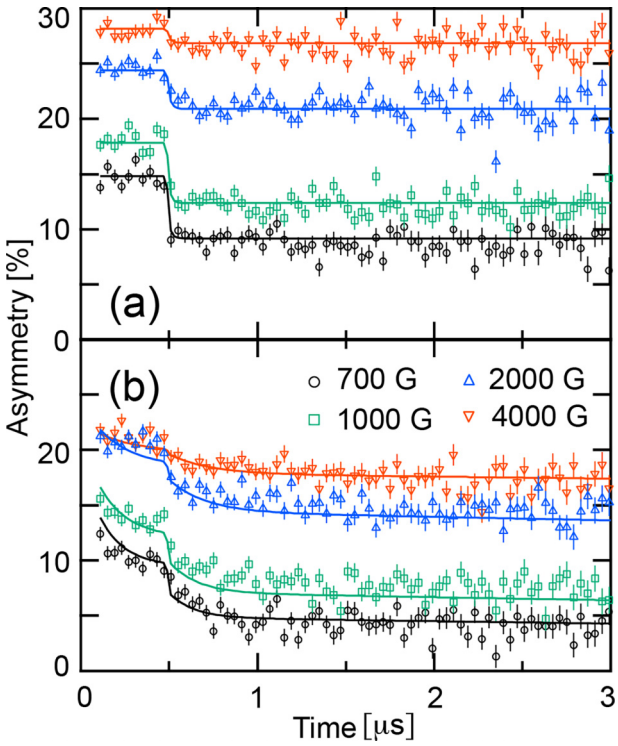

FIG. 4. Photo-μSR time spectra measured at (a) 290 K and (b) 20 K under four representative fields. The pump wavelength was 1.38 and 1.49 eV for (a) and (b) respectively. The laser pulse at $\Delta t = 0.5$ μs generated $\Delta n = 2.6 \times 10^{15}$ and 1.2×10^{16} cm^{-3} for (a) and (b) respectively. Solid lines denote the fit results (see text).

excess carriers, i.e.,

$$\tilde{\Lambda}^{-/0}_{\rm T} = \Lambda^{-/0}_{\rm T} + \Delta n v_{\rm h} \sigma^{-/0}_{\rm T}, \tag{9}$$

$$\tilde{\Lambda}^{0/-}_{\rm T} = \Lambda^{0/-}_{\rm T} + \Delta n v_e \sigma^{0/-}_{\rm T}, \tag{10}$$

$$\tilde{\Lambda}^{0}_{\rm T} = \Lambda^{0}_{\rm T} + \Delta n v_e \sigma^{0}_{\rm T}, \tag{11}$$

$$\tilde{\Lambda}^{0}_{\rm BC} = \Lambda^{0}_{\rm BC} + \Delta n v_e \sigma^{0}_{\rm BC}, \tag{12}$$

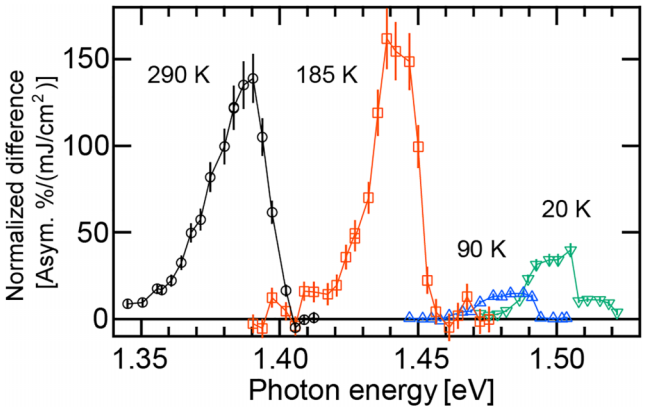

FIG. 5. Photoinduced signals were measured as a function of the pump wavelength at four temperatures. The signal was obtained simply by fitting $A(t)|_{\rm dark} - A(t)|_{\rm light}$ ($t > 0.8$ μs) to a constant, where $A(t)$ is a μSR time spectrum (in %). The obtained value was then normalized by the energy flux. Solid lines are for guiding the viewer's eye.

[4]This calculation accounted for reflections of the transmitted light through the sample, i.e., one from the sample surface (muon side) and another from the Ti window. But since they are nonspecular reflections, the calculated Δn are slightly overestimated (by less than 10%).

where the second term in Eq. (9) describes a Mu_T^- center capturing a hole with the cross section $\sigma_T^{-/0}$ and hole thermal velocity v_h. In the calculation, these additional terms were activated only during the 8-ns pulsed illumination. Although Δn changes with time because of the pulse's temporal profile and the excess carrier decay, we assumed a constant Δn during this period for simplicity in the computation. Similarly to Fig. 1, a global fit was performed on the set of LF-scan data with $\sigma_T^{-/0}$ as the only fit parameter; all other parameters were adapted from the dark measurement. Here we assumed that free excess carriers would dominate the transitions at RT. At 20 K, however, most of them form free excitons according to the Boltzmann distribution because the exciton binding energy in GaAs is 4.2 meV [35]. Hence, to analyze the data in Fig. 4(b), v_e and v_h in the second terms in Eqs. (9)–(12) were replaced by a free exciton thermal velocity v_x. The effective mass of an exciton was assumed to be a sum of the electron and hole effective mass [36]. Obtained fit results are shown in Fig. 4, with $\sigma_T^{-/0} = 3.62(4)$ and $3.77(7) \times 10^{-15}$ cm^2 for 290 and 20 K respectively. The good agreement of the data points and fitting curves at both temperatures supports the validity of the state exchange model [Fig. 2(a)]. The enhanced cross section $\sigma_T^{-/0}$ being an order of magnitude greater than σ_T^0 and $\sigma_T^{0/-}$ can be attributed to the Coulomb interaction between Mu_T^- and h^+. Note that $\sigma_T^{-/0}$ at 290 and 20 K are almost identical; presumably, this cross section only weakly depends on temperature because the Mu_T^- center is known to remain static on the μSR timescale if the temperature is below 500 K [5].

The state exchange model was further tested by measuring the laser power dependence (i.e., the excess carrier density). Figure 6 shows the μSR time spectra for representative excess carrier densities. Here, a LF of 1000 G was applied to the sample to decouple stray fields from the instrument and local fields (e.g., nuclear dipolar interactions). A set of calibrated neutral density filters were used to change the pump laser power incident on the sample. Similarly to the fitting procedure in Fig. 4, global fitting was applied to a set of the Δn-dependent data with $\sigma_T^{-/0}$ as the only fit parameter. The best fit gave $\sigma_T^{-/0} = 3.22(4)$ and $1.81(3) \times 10^{-15}$ cm^2 for 290 and 20 K respectively. This reasonably good agreement with the LF results further supports this model at this level of excess carrier density. Indeed, fit quality for the RT data gets worse if it includes data with $\Delta n > 2.5 \times 10^{15}$ cm^{-3}, where the model requires additional processes. As shown in Eqs. (9)–(12), our model includes a contribution by free holes only in $\tilde{\Lambda}_T^{-/0}$. However, if Δn is sufficiently high, other Mu reactions with the holes can take place, e.g., $Mu_T^0 + h^+ \rightarrow Mu_T^+ + e^- \rightarrow Mu_T^0$; this cyclic process is equivalent to adding an extra term to $\tilde{\Lambda}_T^0$. As shown in Fig. 6(a), the model fails to simulate the high Δn data (dashed line). With lower pumping, reactions by excess electrons are predominant in the exchange processes because of their faster thermal velocity. The contributions by slower holes are negligible in most transition channels except the capture by Mu_T^-. In contrast, deviation from the model was not observed at 20 K [shown in Fig. 6(b)] despite the exciton formation, where a hole should be located in the vicinity of an electron. However, in GaAs these

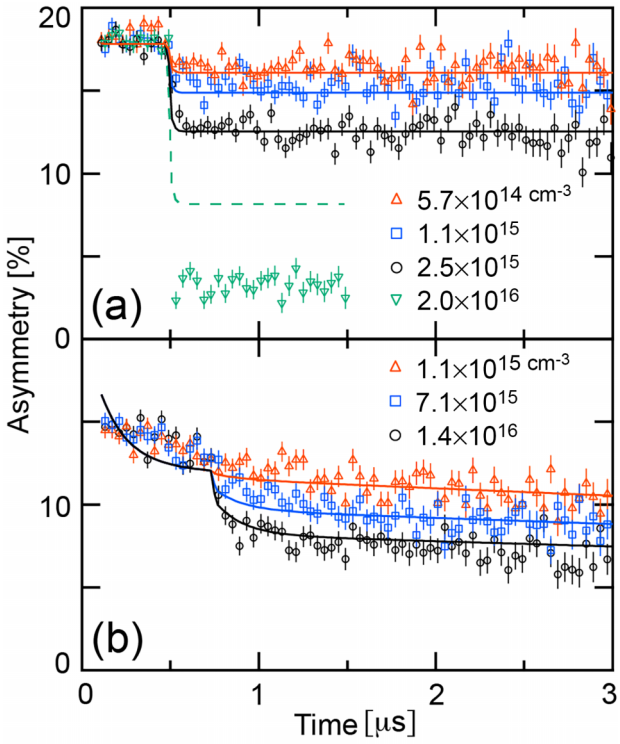

FIG. 6. Laser power dependent photo-μSR time spectra measured at (a) 290 K and (b) 20 K under a 1 kG LF. Time spectra for representative Δn are shown here. Δn were calculated from the measured photon flux and an absorption coefficient for each temperature (see text). The laser pulse timing for (a) and (b) were $\Delta t = 0.5$ and 0.75 μs respectively. Solid lines denote the fit results (see text). The dashed line in (a) denotes a simulated curve for $\Delta n = 2.0 \times 10^{16}$ cm^{-3}.

electron-hole pairs form Wannier-Mott excitons with Bohr radius ≈10 nm. Hence, the absence of the additional contribution by holes could be attributed to the wave function of the bound electron being spatially more extended than that of the hole due to its lighter effective mass; the larger wave packet results in a higher probability of electrons interacting with the Mu centers, which, in turn, dominates the Mu transition mechanism.

V. CONCLUSION

In summary, we identified the Mu state exchange dynamics in *n*-GaAs by fitting the μSR data with the density matrix calculation. Photo-μSR measurements played a key role in testing the model and studying the system response to carrier generation. The model turned out to be rather simple, especially at RT, where the Mu_T center is the predominant species. Our studies not just agreed with the previous studies, but also provided new insight into the underlying Mu state transitions and capture/scattering cross sections of the Mu centers. The Mu behavior learned from this study can be applied to some of the cases with hydrogen, if the difference in their mass is correctly considered. For instance, H atoms in a precursor state probably form the paramagnetic states and go into the state

exchange mechanism before converting to their final stable states. Their scattering cross sections (and transition rates), however, can be different from our measurements because of the difference in zero-point energy.

Looking to future development, first, this study holds the key to understanding the muon signal upon generating electronic spin polarization in n-GaAs [33]. One can optically generate nonequilibrium spin polarization in the conduction electron, where the angular momentum of an absorbed circularly polarized photon is transferred to the electronic spin. GaAs, particularly in n-type, is one of the classic systems in which the spin polarization was demonstrated [37]. Yokoyama *et al.* applied the optical spin orientation and performed a photo-μSR experiment on n-GaAs. They found that the amplitude of optically induced relaxation depended on the direction of the photoexcited electron spin. With electronic spins polarized in the system, one can expect that the electron capture rate of Mu_T^0 to form Mu_T^- should obey the Pauli exclusion principle and depend on the availability of electrons with a correct spin. The state exchange model explained in this study lays a foundation for understanding this phenomenon, which can lead to μSR applications for spintronics studies. Second, we demonstrated that this simulation method and illumination technique are a powerful combination to study Mu dynamics behind μSR relaxation spectra. Although Mu dynamics in Si (and Ge) were extensively studied [5], the picture may not be fully conclusive yet. An application of this method can provide new information with a full state exchange model. This can be the case for other semiconductor systems, such as SiC, where Mu is formed and undergoes state exchange on the timescale of a muon lifetime.

ACKNOWLEDGMENTS

This work was carried out using beam time allocated by the STFC ISIS Facility [22]. Support is acknowledged from the Texas Research Incentive Program (P.W.M., R.L.L.) and the NMU Freshman Fellows Program (M.R.G.). K.Y. and J.S.L. would like to thank Alan J. Drew of Queen Mary University of London for his effort and support in developing the photo-μSR setup in the HiFi spectrometer. Finally, we are grateful for the assistance of a number of technical and support staff in the ISIS facility.

[1] S. M. Myers *et al.*, Hydrogen interactions with defects in crystalline solids, Rev. Mod. Phys. **64**, 559 (1992).
[2] A. R. Peaker, V. P. Markevich, and J. Coutinho, Tutorial: Junction spectroscopy techniques and deep-level defects in semiconductors, J. Appl. Phys. **123**, 161559 (2018).
[3] M. Stavola, in *Semiconductors and Semimetals*, edited by M. Stavola (Elsevier, Amsterdam, 1999), pp. 153–224.
[4] B. D. Patterson, Muonium states in semiconductors, Rev. Mod. Phys. **60**, 69 (1988).
[5] K. H. Chow, B. Hitti, and R. F. Kiefl, in *Semiconductors and Semimetals*, edited by M. Stavola (Elsevier, Amsterdam, 1998), pp. 137–207.
[6] S. F. J. Cox, Muonium as a model for interstitial hydrogen in the semiconducting and semimetallic elements, Rep. Prog. Phys. **72**, 116501 (2009).
[7] P. W. Mengyan, in *Characterisation and Control of Defects in Semiconductors*, edited by F. Tuomisto (IET, London, 2019), pp. 199–262.
[8] C. G. Van de Walle and J. Neugebauer, Hydrogen in semiconductors, Annu. Rev. Mater. Res. **36**, 179 (2006).
[9] R. L. Lichti, K. H. Chow, and S. F. J. Cox, Hydrogen defect-level pinning in semiconductors: The muonium equivalent, Phys. Rev. Lett. **101**, 136403 (2008).
[10] R. L. Lichti, H. N. Bani-Salameh, B. R. Carroll, K. H. Chow, B. Hitti, and S. R. Kreitzman, Donor and acceptor energies for muonium in GaAs, Phys. Rev. B **76**, 045221 (2007).
[11] V. G. Storchak and N. V. Prokof'ev, Quantum diffusion of muons and muonium atoms in solids, Rev. Mod. Phys. **70**, 929 (1998).
[12] R. L. Lichti, in *Semiconductors and Semimetals*, edited by N. H. Nickel (Elsevier, Amsterdam, 1999), pp. 311–371.
[13] S. R. Kreitzman, B. Hitti, R. L. Lichti, T. L. Estle, and K. H. Chow, Muon-spin-resonance study of muonium dynamics in Si and its relevance to hydrogen, Phys. Rev. B **51**, 13117 (1995).
[14] R. Scheuermann, L. Schimmele, J. Schmidl, A. Seeger, Th. Stammler, E. E. Haller, D. Herlach, and J. Major, Muon state dynamics in germanium and silicon, Hyperfine Interact. **105**, 357 (1997).
[15] R. Kadono, A. Matsushita, R. M. Macrae, K. Nishiyama, and K. Nagamine, Muonium centers in crystalline Si and Ge under illumination, Phys. Rev. Lett. **73**, 2724 (1994).
[16] R. Scheuermann, J. Major, A. Seeger, L. Schimmele, J. Schmidl, and D. Herlach, The interaction of positive muons with photogenerated charge carriers in crystalline silicon, Phys. B: Condens. Matter **289-290**, 534 (2000).
[17] I. Fan, K. H. Chow, B. Hitti, R. Scheuermann, W. A. MacFarlane, A. I. Mansour, B. E. Schultz, M. Egilmez, J. Jung, and R. L. Lichti, Optically induced dynamics of muonium centers in Si studied via their precession signatures, Phys. Rev. B **77**, 035203 (2008).
[18] K. Yokoyama, J. S. Lord, J. Miao, P. Murahari, and A. J. Drew, Photoexcited muon spin spectroscopy: A new method for measuring excess carrier lifetime in bulk silicon, Phys. Rev. Lett. **119**, 226601 (2017).
[19] T. Prokscha, K. H. Chow, E. Stilp, A. Suter, H. Luetkens, E. Morenzoni, G. J. Nieuwenhuys, Z. Salman, and R. Scheuermann, Photo-induced persistent inversion of germanium in a 200-nm-deep surface region, Sci. Rep. **3**, 2569 (2013).
[20] T. Prokscha, K. H. Chow, Z. Salman, E. Stilp, and A. Suter, Direct Observation of hole carrier-density profiles and their light-induced manipulation at the surface of Ge, Phys. Rev. Appl. **14**, 014098 (2020).
[21] J. S. Lord *et al.*, Design and commissioning of a high magnetic field muon spin relaxation spectrometer at the ISIS pulsed neutron and muon source, Rev. Sci. Instrum. **82**, 073904 (2011).
[22] K. Yokoyama, J. S. Lord, P. W. Mengyan, M. R. Goeks, and R. L. Lichti, Can photo-MuSR method measure

carrier recombination lifetime in direct gap semiconductors? STFC ISIS Neutron and Muon Source Data Journal, 2019, doi:10.5286/ISIS.E.RB1920737.

[23] K. Yokoyama *et al.*, The new high field photoexcitation muon spectrometer at the ISIS pulsed neutron and muon source, Rev. Sci. Instrum. **87**, 125111 (2016).

[24] K. Yokoyama, J. S. Lord, J. Miao, P. Murahari, and A. J. Drew, Decoupling bulk and surface recombination properties in silicon by depth-dependent carrier lifetime measurements, Appl. Phys. Lett. **118**, 252105 (2021).

[25] R. Kadono, A. Matsushita, K. Nagamine, K. Nishiyama, K. H. Chow, R. F. Kiefl, A. MacFarlane, D. Schumann, S. Fujii, and S. Tanigawa, Charge state and diffusivity of muonium in *n*-type GaAs, Phys. Rev. B **50**, 1999 (1994).

[26] J. S. Lord, Computer simulation of muon spin evolution, Phys. B: Condens. Matter **374-375**, 472 (2006).

[27] See Supplemental Material at http://link.aps.org/supplemental/10.1103/PhysRevResearch.6.033140 for representative source codes and details of the fitting procedure.

[28] K. H. Chow *et al.*, Structure of negatively charged muonium in *n*-type GaAs, Phys. Rev. B **51**, 14762 (1995).

[29] For example, see D. A. Neamen, *Semiconductor Physics and Devices: Basic Principles*, 4th ed. (McGraw-Hill Education, New York, 2011), p. 133.

[30] K. H. Chow, B. Hitti, R. F. Kiefl, S. R. Dunsiger, R. L. Lichti, and T. L. Estle, Diffusion and charge dynamics of negatively charged muonium in *n*-type GaAs, Phys. Rev. Lett. **76**, 3790 (1996).

[31] R. Kadono, R. F. Kiefl, J. H. Brewer, G. M. Luke, T. Pfiz, T. M. Riseman, and B. J. Sternlieb, Quantum diffusion of muonium in GaAs, Hyperfine Interact. **64**, 635 (1991).

[32] R. F. Kiefl, M. Celio, T. L. Estle, G. M. Luke, S. R. Kreitzman, J. H. Brewer, D. R. Noakes, E. J. Ansaldo, and K. Nishiyama, Determination of the electronic structure of anomalous muonium in GaAs from nuclear hyperfine interactions, Phys. Rev. Lett. **58**, 1780 (1987).

[33] K. Yokoyama *et al.*, Detection of conduction electron spin polarization in n-GaAs by negative muonium, Phys. Procedia **30**, 231 (2012).

[34] M. D. Sturge, Optical absorption of gallium arsenide between 0.6 and 2.75 eV, Phys. Rev. **127**, 768 (1962).

[35] S. B. Nam, D. C. Reynolds, C. W. Litton, R. J. Almassy, T. C. Collins, and C. M. Wolfe, Free-exciton energy spectrum in GaAs, Phys. Rev. B **13**, 761 (1976).

[36] D. C. Mattis and J.-P. Gallinar, What is the mass of an exciton? Phys. Rev. Lett. **53**, 1391 (1984).

[37] J. M. Kikkawa and D. D. Awschalom, Resonant spin amplification in *n*-type GaAs, Phys. Rev. Lett. **80**, 4313 (1998).